coatings

MDPI

Article

The Micro-Scaled Characterization of Natural Terrestrial Ferromanganese Coatings and Their Semiconducting Properties

Xiaoming Xu, Hongrui Ding, Yan Li, Haoran Wang and Anhuai Lu *

Beijing Key Laboratory of Mineral Environmental Function, School of Earth and Space Sciences, Peking University, Beijing 100871, China; xmxu@pku.edu.cn (X.X.); dhr_100@163.com (H.D.); pku_ly@163.com (Y.L.); hrwang_pku@126.com (H.W.)

* Correspondence: ahlu@pku.edu.cn; Tel./Fax: +86-10-6275-3555

Received: 22 June 2020; Accepted: 10 July 2020; Published: 11 July 2020

Abstract: Different types of ferromanganese coatings were collected from the Chinese mainland to study their mineralogical characteristics and semiconducting properties. Measurements, including by optical microscope, scanning electron microscope, energy dispersive X-ray spectroscopy, micro-Raman spectrometer and transmission electron microscope, were employed to study their morphology, mineral assemblage, element abundance and distribution patterns. Soil Fe coatings are mainly composed of Al-rich hematite and clays. Soil Fe/Mn coatings can be divided into an outer belt rich in birnessite and an inner belt rich in hematite, goethite, ilmenite and magnetite. Goethite is the only component of rock Fe coatings. Rock Fe/Mn coatings mainly consist of birnessite and hematite, and alternating Fe/Mn-rich layers and Fe/Mn-poor layers can be observed. Powders were scraped off from the topmost part of ferromanganese coatings to conduct laboratory photochemical experiments. The photocurrent–time behavior indicates that natural coating electrodes exhibit an immediate increase in photocurrent intensity when exposed to light irradiation. Natural coatings can photo-catalytically degrade 14.3%–58.4% of methyl orange in 10 h. Under light irradiation, the photocurrent enhancement and organic degradation efficiency of the rock Fe/Mn coating, which has a close intergrowth structure of Fe and Mn components, is most significant. This phenomenon is attributed to the formation of semiconductor heterojunctions, which can promote the separation of electrons and holes. Terrestrial ferromanganese coatings are common in natural settings and rich in semiconducting Fe/Mn oxide minerals. Under solar light irradiation, these coatings can catalyze important photochemical processes and will thus have an impact on the surrounding environment.

Keywords: ferromanganese coatings; semiconducting minerals; photocatalysis; methyl orange

1. Introduction

Fe and Mn are the most abundant transition elements on Earth and can form different oxide mineral phases. So far, more than 16 Fe oxide minerals and 30 Mn oxide minerals have been identified in a wide variety of geological settings [1,2]. Among various carriers rich in Fe/Mn oxides, soil cutan and rock varnish are the most representative deposits which have been extensively studied and reported in the literature. Soil cutan covers the surface of large soil blocks and mineral grains. However, the mineralogy of soil cutan has not been totally revealed due to the fine grains, poor crystallinity and low content of Mn oxides. It is reported that Mn oxide minerals exhibit several phases, including birnessite, lithiophorite, todorokite, vernadite, hollandite, etc., among which lithiophorite and brinessite are the most frequently reported ones [3–5]. Huang et al. [6,7] systematically studied the elemental distribution patterns and morphology of soil cutan in China and indicated that cutan can be easily

distinguished by outer Mn-rich and inner Fe-rich regions. Rock varnish covers a diversity of lithologies and exhibits a layered structure. It is mainly composed of poorly crystallized Fe/Mn oxides and clay minerals [8,9]. According to the literature, hematite and birnessite are the dominating mineral phases of Fe/Mn oxides [9–14]. Alternating dark and light layers, which arise from Mn content fluctuations, can be observed in the cross-section profile of varnish [15]. Terrestrial ferromanganese coatings have important environmental significance. For example, the Mn content fluctuations within the coating profile can be used to reflect climate change during its formation [6,16]; varnish micro-laminations can be used to date ancient petroglyphs carved on rock surfaces [17]; and Mn oxides with good ion exchange and adsorption capabilities can scavenge heavy metals in sediments and soils [7,18].

Natural Fe/Mn oxide minerals are also semiconducting materials. Fe oxide minerals have a band gap of 2.0–2.5 eV and Mn oxide minerals have a band gap of 1.0–1.8 eV [19], which allow them to produce active electron–hole pairs under solar light irradiation. The Fe/Mn oxide minerals involved in photocatalytic reactions can exert great influence on the surrounding environment. In the laboratory, synthetic birnessite can catalyze the photooxidation of a wide range of organics, including indigo carmine [20], benzene [21,22] and phenolic compounds [23–25]. Birnessite-type MnO_2 is also known to photocatalyze water splitting to generate oxygen [26,27]. Georgiou et al. [28] reported reactive oxygen species (ROSs) formed by the photocatalysis of metal oxide minerals, which contributes to the circuit of the biogeochemical carbon cycle in arid regions. The doping of Fe/Mn components can greatly improve the photoelectrochemical performance of CdSe films [29,30]. Density functional theory study indicates that Mn vacancies can promote the photoreductive dissolution of hexagonal birnessite and the release of Mn^{2+} [31]. The reported evidence suggests that the semiconducting properties of ferromanganese coatings have great potential in shaping modern terrestrial environments, however, little work has focused on this research field.

In this paper, we collected different types of ferromanganese coatings, including soil Fe coatings, soil Fe/Mn coatings, rock Fe coatings and rock Fe/Mn coatings, to study their mineralogical features and semiconducting performances. Thin sections were prepared and their morphology was observed using an optical microscope (OP) and scanning electron microscope (SEM). The energy dispersive X-ray spectroscopy (EDS) mapping of thin sections was carried out to investigate their element abundance and distribution patterns. The Fe/Mn oxide mineral assemblage in coatings was determined by micro-Raman spectroscopy. A transmission electron microscope (TEM) was used to provide the crystallographic information of Fe/Mn oxide minerals in coatings on the nanometer scale. In order to test the semiconducting properties of natural ferromanganese coatings, powders were scraped off the topmost part of these coatings to conduct photocurrent measurements and the photocatalytic degradation of methyl orange (MO). Our mineralogical analysis and laboratory experiments can provide insights for the photochemical performance of natural ferromanganese coatings, and deepen the understanding of their influence on the surrounding environment.

2. Materials and Methods

2.1. Sample Collection and Preparation

Soil coatings were collected from topsoil which was not covered by vegetation and was continuously irradiated by solar light in Haikou City, Hainan Province, China. The surface of the soil blocks was yellow, red and black with a particle size of 100–500 μm, thus indicating different kinds of components in these coatings. Rock coatings were collected from the desert in Hami City, Sinkiang Province, China. The coatings grow on host rock pebbles with diameters of several decimeters. The pebbles spread on the desert pavement and black crust could be discovered on the top.

All the samples were impregnated and solidified by using polyester resin. Then, samples were cut along the vertical direction of the coating surface into the substrate and burnished into thin sections to obtain a thickness of about 30 μm. Morphological observation was conducted on thin sections under a polarizing microscope.

Deep and smooth micro-basins on the soil block and rock surface were located for the preparation of powders, because these coatings can be thick and the incorporation of substrate composition can hence be reduced. We scraped off the topmost part of the coatings and prepared fine-grained powders by using a high-purity quartz rod. For each type of coating, 50 mg powders were mixed with anhydrous ethanol (400 μL) and Nafion (10 μL) to make the mineral paste. Then, the mineral paste was evenly smeared on a transparent conductive fluorine-doped tin oxide (FTO) substrate. The coating electrodes were used for photocurrent measurements after drying for 10 h in air.

2.2. Micro-Raman Spectroscopy

Most Fe/Mn oxide minerals are poorly crystalized with small sizes. Therefore, they are difficult to accurately identify by traditional methods like XRD. Vibrational spectroscopy, such as Raman spectra, is sensitive to amorphous components and those with a short-range order, which can yield a more complete and reliable result [32,33]. Micro-Raman spectra analysis of sample thin sections can exclude the interference of substrate. The spectra were recorded using a micro-Raman spectrometer (inVia Reflex, Renishaw, UK) with a laser excitation wavenumber of 785 nm to avoid fluorescence signals. Spectra acquisition was performed under a 50× Leica objective lens (NA = 0.75) across the 100–1300 cm^{-1} wavenumber range, and the spot size was 1 μm. The integration time for individual measurement was 5 s. Accumulation times ranged from 3 to 10, which was based on the spectrum quality and signal to noise ratio. The Raman test had a wavenumber resolution of less than 1 cm^{-1}.

2.3. Scanning Electron Microscope

Representative sample thin sections were chosen and sputtered with Cr for analysis using a Quanta 650 FEG field emission SEM with EDS for chemical analysis (Hillsboro, OR, USA). Morphological observation was carried out by the application of secondary electron and back-scattered electron detectors. The chemical composition of different ferromanganese coatings was investigated with EDS using automated quantitative elemental analysis mode. Element content was given as weight percentage. EDS mapping was conducted to investigate the elemental distribution patterns. The SEM/EDS analysis was carried out at an acceleration voltage of 14 kV.

2.4. Transmission Electron Microscope

TEM coupled with EDS equipment and selected area electron diffraction were used to provide crystallographic information of Fe/Mn minerals in coatings. After ultrasonic dispersion, 0.1 mL alcohol, which contained coating powders, were dripped on a mesh copper grid. The alcohol was then absorbed by filter paper from the other side of the grid. The mesh copper grid was placed into the sample holder which was attached to the specimen stage. The experiment was carried out with a JEM-2100F TEM (JEOL, Aichi, Japan), operating at 200 kV. The point resolution was 0.19 nm.

2.5. Photoelectrochemical Measurements

Photocurrent measurements were carried out with a set-up consisting of a cylindrical quartz glass reactor. A white LED lamp with a three-electrode configuration was used to simulate sun light irradiation of the samples. A platinum sheet (1 cm × 1 cm) was used as the counter electrode. The reference electrode was an Ag/AgCl (4 M KCl) electrode and working electrode was the natural coating powders covered in FTO substrate. To maintain sufficient solution conductivity, 0.5 mol/L Na_2SO_4 was chosen as the supporting electrolyte. An area of 2.5 × 3 cm^2 of the natural coating electrodes was irradiated by the lamp from the back side, and the incident intensity was adjusted to 120 mW/cm^2. The cooling of the reactor was established by means of air flow using an incorporated fan. A potential of 0.8 V (vs. Ag/AgCl) was applied in the photocurrent experiments.

In the MO degradation experiments, 10 mg coating powders were added into the quartz glass reactor, which contained 100 mL MO solution with 4.0 mg/L initial concentration. The pH of the solution was fixed at 7.0 using a Mettler Toledo pH meter. The light source configuration was the

same as for the photocurrent experiments described above. One milliliter of suspension was collected from the reactor at regular time intervals (30 min) to determine the residual concentration of MO. The concentration of MO was determined by measuring the absorbance at 476 nm with a diode array UV-2102 PC spectrophotometer (Thermo Fisher Scientific, Waltham, MA, USA). This maximum absorbance peak was attributed to the azo bond of MO [34]. The assays were repeated twice to contribute to a data error ≤ 2%. The total reaction time was 600 min. The efficiency of MO degradation was estimated by this equation:

$$\text{MO degradation ratio} = (1 - C_t/C_0) \times 100\% \quad (1)$$

Here, C_0 (mg/L) and C_t (mg/L) stand for the MO concentration at the beginning and at time t, respectively.

3. Results

3.1. Mineralogical Characteristics of Soil Ferromanganese Coatings

The soil Fe coating is red or yellow in color, wrapping large soil blocks and mineral clasts like quartz (Figure 1a,b). The observation of thin sections indicates that the thickness of the coating is ~10–50 μm (Figure 1c). In the SEM image, the Fe coating is porous and features holes with sizes less than 1 μm (Figure 1d). The elemental Fe distribution correlates with the Al distribution (Figure 1e,f), indicating that these two elements may co-exist in a common mineral phase. The Fe content in soil Fe coatings can be enriched to 3.59 wt.%–17.42 wt.% (Table S1). Si is much more abundant in the substrate when compared with its low content in the coating (Figure 1g). The micro-Raman spectra analysis indicates that the Fe oxide mineral in the coating is mainly hematite. Three diagnostic Fe–O symmetric bending vibration modes can be discriminated at 297, 409 and 609 cm^{-1} (Figure 1h). Hematite belongs to the $D_{3d}{}^6$ crystal space group and seven phonon lines are expected in the Raman spectrum, namely two A_{1g} modes and five E_g modes [35]. Commonly, the 293 and 297 cm^{-1} bands are only resolved at 100 K or less [36]. The shoulder band at 498 cm^{-1} in our results is too weak to be detected. The diagnostic Raman bands at 225 and 247 cm^{-1} in our results are missing due to Al substitution for Fe, as indicated by the EDS mapping. According to the literature [37], the Raman intensity of these two bands decreases sharply with growing Al substitution for Fe in hematite. This variation is caused by a local disorder correlated to the insertion of Al^{3+} ions into the FeO_6 octahedron [37].

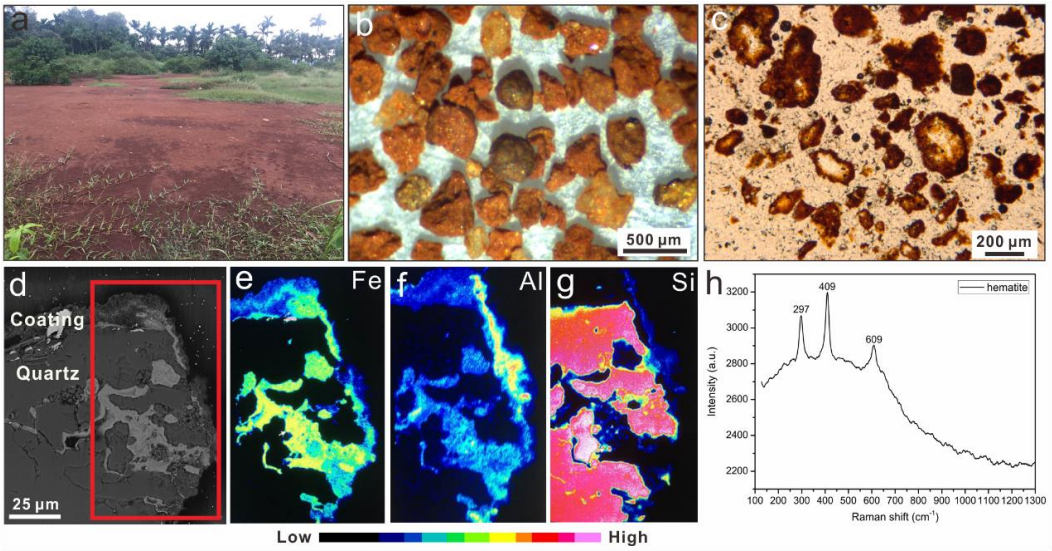

Figure 1. Field occurrence (**a**), hand specimen (**b**), optical image (**c**), back-scattered image (**d**), elemental distribution patterns (**e**–**g**) and Raman spectrum (**h**) of soil Fe coatings. The rectangle in panel (**d**) indicates the EDS mapping region.

The soil Fe/Mn coating is black in color, covering the surface of soil blocks or mineral clasts (Figure 2a). The observation of thin sections indicates that the coating is ~30–50 μm in thickness (Figure 2b). The coating consists of different layers. The outer layer is rich in Mn with a thickness of ~30 μm, while the inner layer is rich in Fe with a thickness of ~20 μm. EDS mapping indicates a distinct boundary between these two layers (Figure 2d,e). Si and Al are not enriched in this coating compared with their high contents in the substrate (Figure 2f,g). The Mn content can be enriched to 9.77 wt.%–11.57 wt.% in the outer layer (Table S2). Micro-Raman spectra analysis reveals that the Mn phase is birnessite. Three diagnostic Mn–O stretching vibration modes at 514, 589 and 649 cm^{-1} (A_g phonon species) and one Mn–O bending vibration mode at 292 cm^{-1} (B_g phonon species) can be observed (Figure 3a). The Fe-rich layer exhibits several different phases, including hematite, goethite and ilmenite (Figure 3b–d). Four Raman bands of hematite at 222, 287, 402 and 602 cm^{-1} can be observed (Figure 3b). The three Raman bands at 301, 394 and 553 cm^{-1} can be attributed to goethite (Figure 3c). Raman signals of ilmenite are characterized by one sharp band at 682 cm^{-1} and two weak bands at 227 and 375 cm^{-1} (Figure 3d).

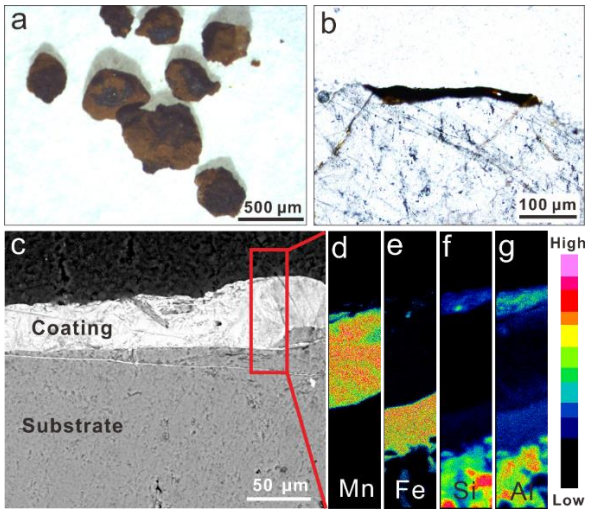

Figure 2. Hand specimen (**a**), optical image (**b**), back-scattered image (**c**) and elemental distribution patterns (**d**–**g**) of soil Fe/Mn coating. The rectangle in panel (**c**) indicates the EDS mapping region.

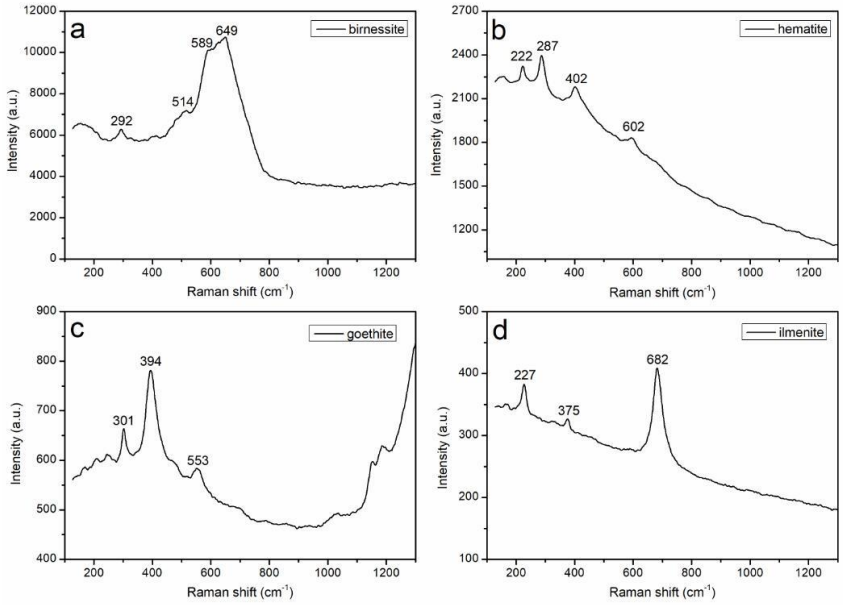

Figure 3. Raman spectra of the soil Fe/Mn coating. (**a**) Birnessite; (**b**) hematite; (**c**) goethite; (**d**) ilmenite.

Under TEM, the EDS mapping was carried out to locate the regions of Fe/Mn-rich particles. The EDS data reveal an area with an Mn content of 23.20% (Figure 4a,b). There are many Si and Al components in this region because the incorporation of clays could not be avoided during sample preparation. Ba is also enriched in this region, mainly because of its good affinity to Mn oxide minerals (Figure 4b). Mn oxide minerals are commonly very small with poor crystallinity. Some weak and discontinuous lattice fringes can be discriminated in the crystalline domains (Figure 4c). A region of this lattice photograph is chosen for fast Fourier transform (FFT), inverse FFT and calibration (Figure 4d). The *d* spacing value of 0.72 nm can be assigned to the crystal face of (001) of birnessite, and the diffraction pattern shows a clear hexagonal lattice (Figure 4d).

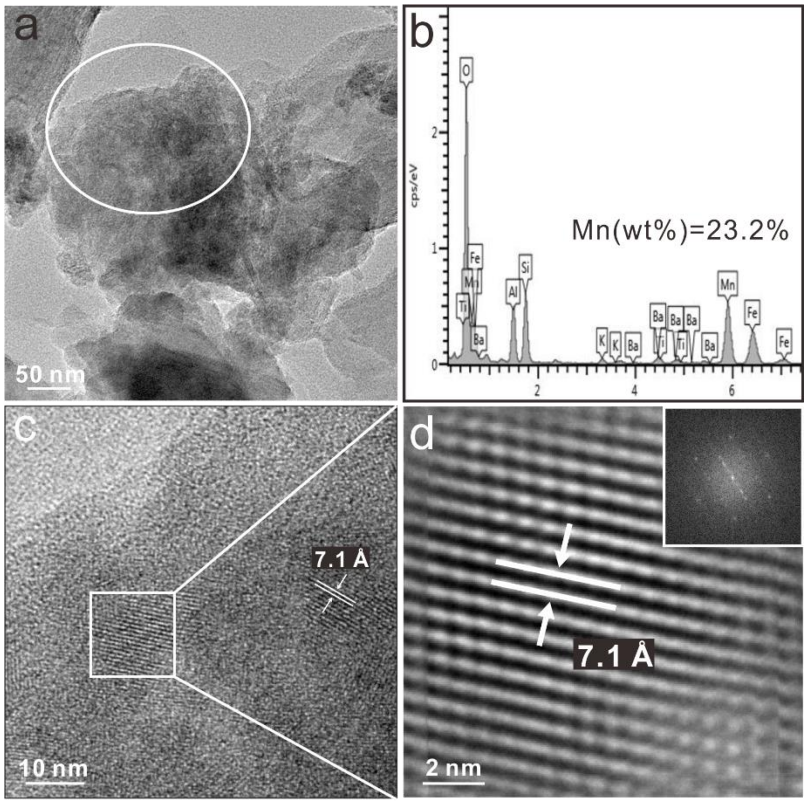

Figure 4. TEM morphology (**a**), chemical composition (**b**), lattice photograph (**c**) and diffraction pattern (**d**) of Mn-rich grains in the soil Fe/Mn coating. Panel (**b**) shows the chemical composition of the selected oval region in panel (**a**). The lattice fringes and diffraction pattern in panel (**d**) are the FFT (fast Fourier transform) and inverse FFT results of the selected rectangular region in panel (**c**).

Similarly, an area with an Fe content of 51.70% is discovered (Figure 5a,b). This particle is an aggregate composed of different Fe nanocrystals, demonstrating a granular morphology with a diameter of ~70 nm (Figure 5a). A region with clear lattice fringes is selected (Figure 5c), in which a broad *d* spacing value of 0.42 nm is most obvious (Figure 5c,d) and can be assigned to the lattice face of (110) of goethite. The parallel lattice fringes in Figure 5e,f display a *d* spacing value of 0.27 nm, which can be attributed to the crystal face of (020) of hematite. Under TEM, we also locate one single crystal of magnetite (Figure 6a). Lattice fringes in Figure 6b are obvious and continuous with a *d* spacing value of 0.29 nm, and they can be assigned to the crystal face of (220) of magnetite. The electron diffraction pattern shows a clear cubic lattice (Figure 6c), which is consistent with the crystal structure of magnetite.

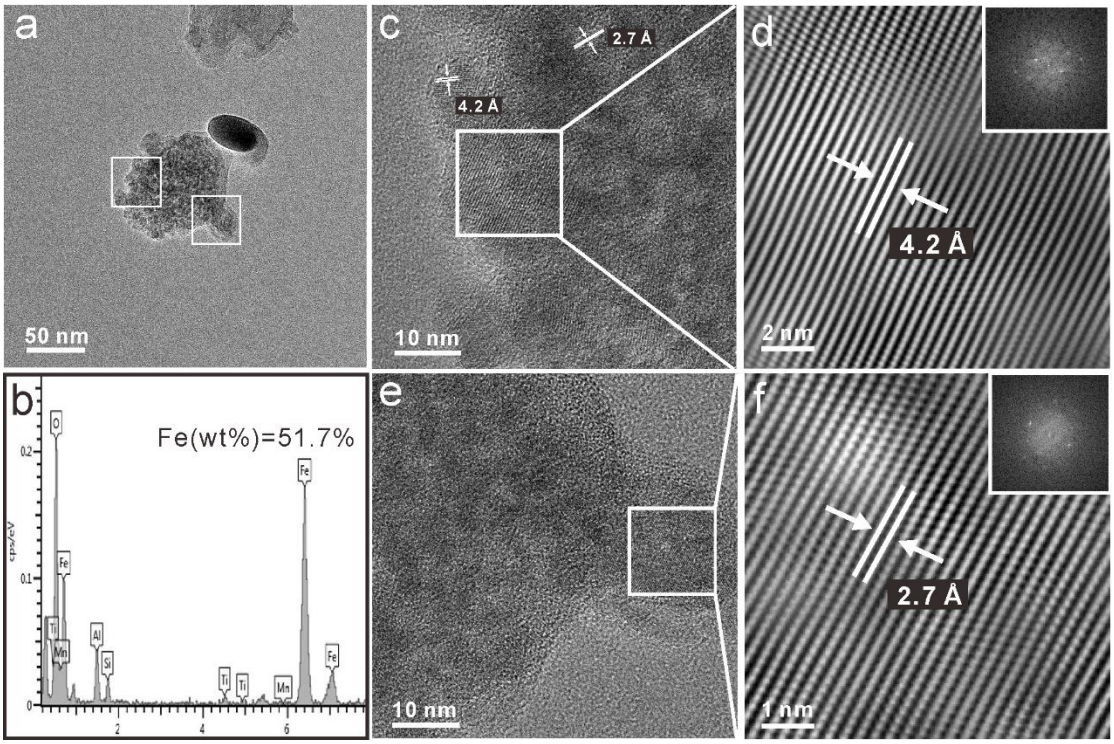

Figure 5. TEM morphology (**a**), chemical composition (**b**), lattice photograph (**c**,**e**) and diffraction pattern (**d**,**f**) of Fe-rich grains in the soil Fe/Mn coating. Panel (**b**) shows the chemical composition of the Fe-rich nanocrystal aggregate. The lattice fringes and diffraction patterns in panels (**d**) and (**f**) are the FFT and inverse FFT results of selected rectangular regions in panels (**c**) and (**e**), respectively.

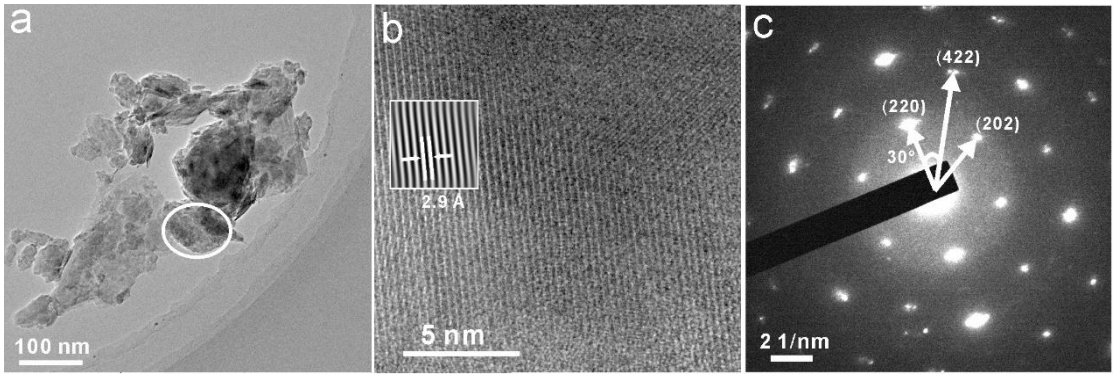

Figure 6. TEM morphology (**a**), lattice photograph (**b**) and selected area electron diffraction pattern (**c**) of magnetite in the soil Fe/Mn coating.

3.2. Mineralogical Characteristics of Rock Ferromanganese Coatings

The rock Fe coating is black in color, covering sandstone with a thickness of ~50 μm (Figure 7a). Raman spectra indicate that the Fe oxide mineral in this coating is goethite. Five diagnostic Raman bands of goethite can be observed, including two sharp bands at 299 and 397 cm^{-1}, and three weak bands at 242, 477 and 553 cm^{-1} (Figure 7b). EDS mapping is carried out in the rectangular region in Figure 7c and results indicate that the Fe distribution pattern matches the morphology of the Fe coating in the back-scattered image (Figure 7d). The mapping results and EDS data reveal that the Si and Al amount is very low in this coating (Figure 7e,f, Table S3) and the Fe content can be enriched to 58.18 wt.%–61.61 wt.% (Table S3).

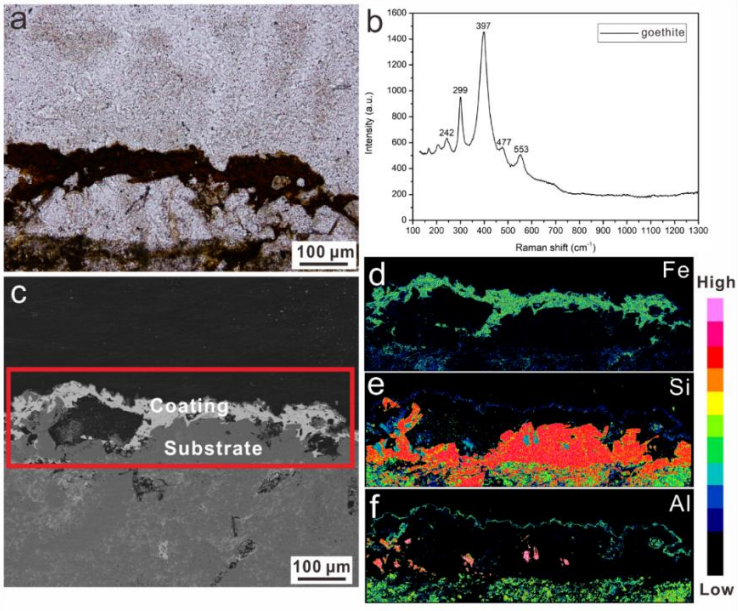

Figure 7. Optical image (**a**), Raman spectrum (**b**), back-scattered image (**c**) and elemental distribution patterns (**d**–**f**) of the rock Fe coating. The rectangle in panel (**c**) indicates the EDS mapping region.

The rock Fe/Mn coating in this research is commonly known as rock varnish, which covers quartzite and granite. The coating is black (Figure 8a,b) and has a thickness of ~30–50 μm (Figure 8c). EDS mapping indicates that Mn and Fe are distributed throughout the whole sample profile (Figure 8e,f), and there is no clear boundary between the Mn and Fe components. Alternating Mn-rich and Mn-poor layers can be discovered in this coating with a thickness of ~25 μm, and each layer is ~2–4 μm wide. Some common petrogenetic elements, like Si, are not enriched in this coating contrary to their high contents in the substrate (Figure 8g). The Mn content can be enriched to 11.73 wt.%–27.61 wt.% and the Fe content can be enriched to 5.30 wt.%–13.98 wt.% in the rock Fe/Mn coating (Table S4). Micro-Raman spectra analysis reveals that the Mn oxide mineral in the varnish is birnessite. Two diagnostic Mn–O stretching vibration modes at 592 and 658 cm^{-1} and one Mn–O bending vibration mode at 296 cm^{-1} can be observed (Figure 9a). According to the literature [38], the Raman band at 145 cm^{-1} (Figure 9a) can be attributed to the stretching modes of the interlayer cation groups (NaO_6 or KO_6) in birnessite. The Fe oxide mineral in the varnish is mainly hematite. Diagnostic Raman bands of hematite are located at 224, 292, 408, 475 and 607 cm^{-1} (Figure 9b).

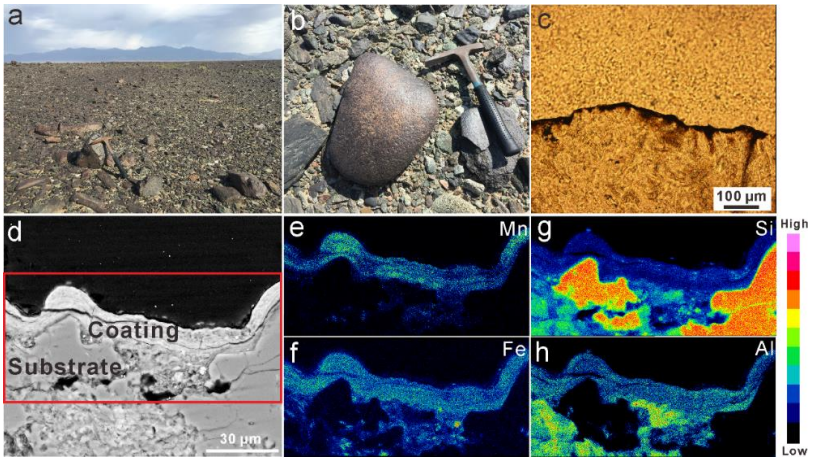

Figure 8. Field occurrence (**a**), hand specimen (**b**), optical image (**c**), back-scattered image (**d**) and elemental distribution patterns (**e**–**h**) of the rock Fe/Mn coating. The rectangle in panel (**d**) indicates the EDS mapping region.

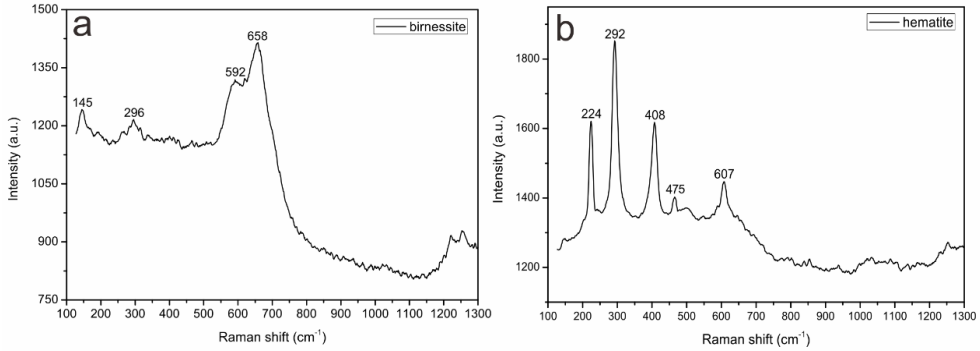

Figure 9. Raman spectra of the rock Fe/Mn coating. (**a**) Birnessite; (**b**) hematite.

The EDS mapping was carried out to seek the regions of the elements of interest. A clear crystalline domain with granular morphology was found (Figure 10a), and Mn was enriched to 22.03% in this area (Figure 10b). A small region of this lattice photograph was chosen for FFT, inverse FFT and calibration (Figure 10c). The *d* spacing value of 0.72 nm can be attributed to the crystal face of (001) of birnessite (Figure 10d), and it is the interlayer distance of adjacent MnO_6 octahedron layers. Similarly, two regions with an Fe content of 78.46% and 39.39% are located (Figure 10f,j). The former one demonstrates a columnar morphology and is composed of small Fe nanocrystals (Figure 10e). A region which shows clear lattice fringes is selected (Figure 10g), in which *d* spacing values of 0.25 and 0.27 nm can be discriminated (Figure 10g,h) and are attributed to the lattice faces of (110) and (104) of hematite, respectively. The parallel lattice fringes in Figure 10k show a broad *d* spacing value of 0.5 nm, which can be assigned to the crystal face of (020) of goethite (Figure 10l).

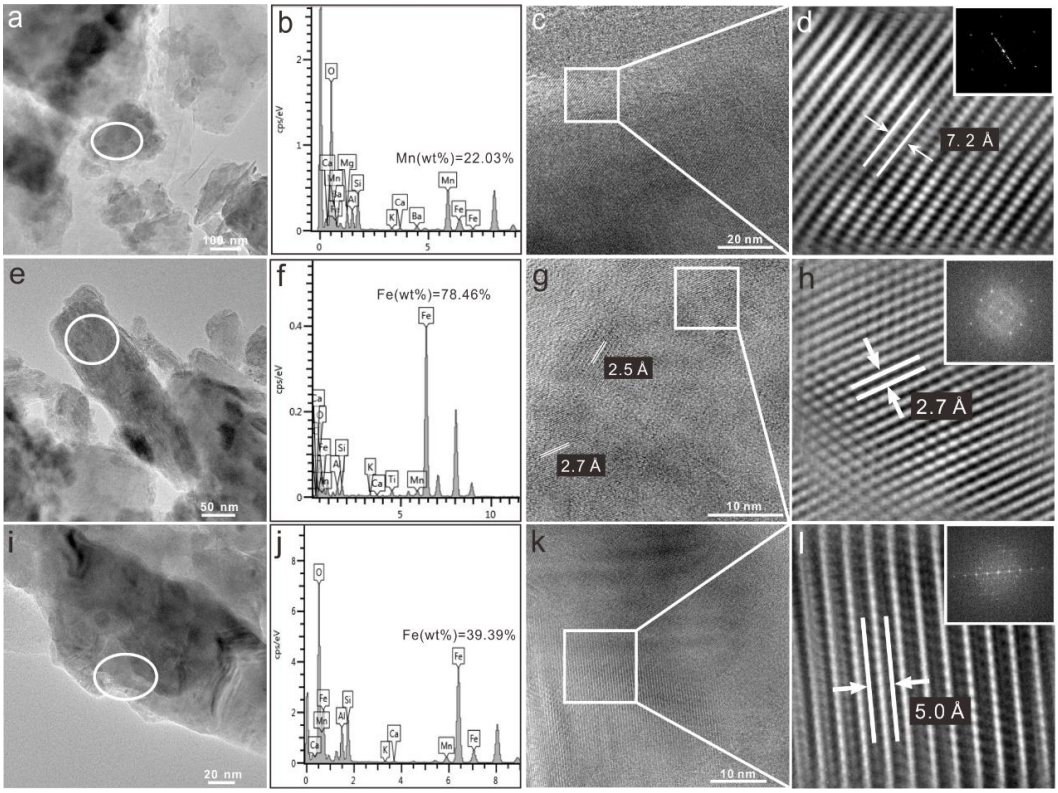

Figure 10. TEM morphology (**a**,**e**,**i**), chemical composition (**b**,**f**,**j**), lattice photograph (**c**,**g**,**k**) and diffraction pattern (**d**,**h**,**l**) of Mn-rich and Fe-rich grains in the rock Fe/Mn coating. Panels (**b**,**f**) and (**j**) show the chemical composition of the selected oval regions in panels (**a**,**e**) and (**i**), respectively. The lattice fringes and diffraction patterns in panels (**d**,**h**) and (**l**) are the FFT and inverse FFT results of selected rectangular regions in panels (**c**,**g**) and (**k**), respectively.

3.3. Semiconducting Properties of Natural Ferromanganese Coatings

The capability of converting light energy to electricity was confirmed by photochemical experiments. The photocurrent–time behavior of natural ferromanganese coating electrodes demonstrates that photocurrent intensity immediately increases when light is turned on and decreases back to the baseline level when light is switched off under a given voltage of 0.8 V (vs. Ag/AgCl) (Figure 11). The dark currents in all cases were negligible, while during the irradiation period, enhanced, sensitive and stable current signals were recorded. This phenomenon indicates that simulated sunlight facilitated the formation of more free electrons from semiconducting Fe/Mn oxide minerals. In particular, the rock Fe/Mn coating and soil Fe/Mn coating produced stable photocurrent densities of 18.5 and 16.5 μA/cm^2 under irradiation, respectively, showing the best photoelectric conversion efficiency compared with other counterparts. The soil Fe coating and rock Fe coating only yield enhanced photocurrent densities of 3.5 and 2.0 μA/cm^2, respectively.

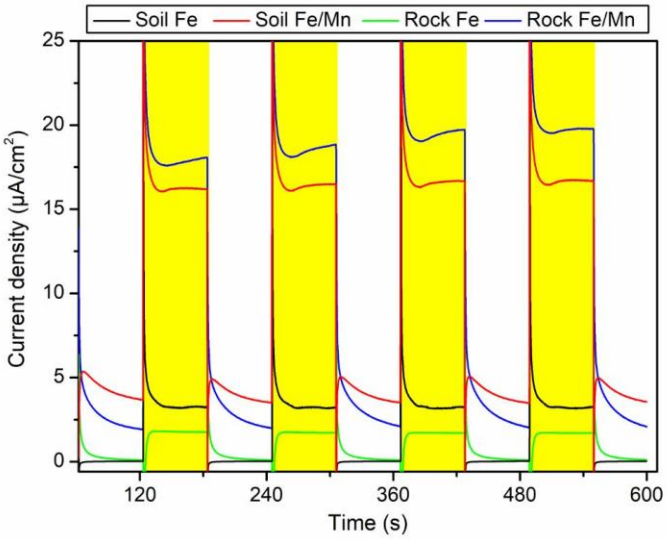

Figure 11. Photocurrent–time behavior of the soil Fe coating, soil Fe/Mn coating, rock Fe coating and rock Fe/Mn coating electrodes. The yellow regions indicate when the light is turned on.

Methyl orange dye is a model compound to evaluate the activity of photocatalysts. During the photochemical experiments, two main processes could have contributed to the decrease in the MO concentration. The composition of natural ferromanganese coatings is complicated and inhomogeneous, and MO can hence be physically adsorbed on clays, Fe/Mn oxide minerals and even on the experimental device. The second is the photocatalysis process mediated by Fe/Mn oxide minerals in natural coatings. Under irradiation, electrons are excited from the valence band (VB) of semiconducting minerals to the conduction band (CB), thus leaving photo-generated holes in the VB with good oxidizing capability. Consequently, MO can be scavenged by the holes or free radicals [28]. Therefore, control groups were set up during our experiments (Figure 12). These four types of natural ferromanganese coatings demonstrate similar trends in MO degradation. In the presence of natural coating powders, the concentration of MO decreases with time in both light and dark systems. The degradation efficiency is much better in the light system in comparison with the dark system. This observation indicates that the photocatalytic degradation process is more effective than physical adsorption. After a reaction time of 600 min, the degradation ratios of MO in the soil Fe coating light system and dark system are 34.7% and 6.8%, respectively, which means the degradation ratio of the photocatalytic process is 27.9% (Figure 12a). Similarly, the degradation ratios of the photocatalytic processes in the soil Fe/Mn coating, rock Fe coating and rock Fe/Mn coating systems are 43.3%, 14.3% and 58.4%, respectively (Figure 12). The rock Fe/Mn coating, which has a close intergrowth structure of Mn and Fe components, exhibits the best performance in MO degradation (Table 1).

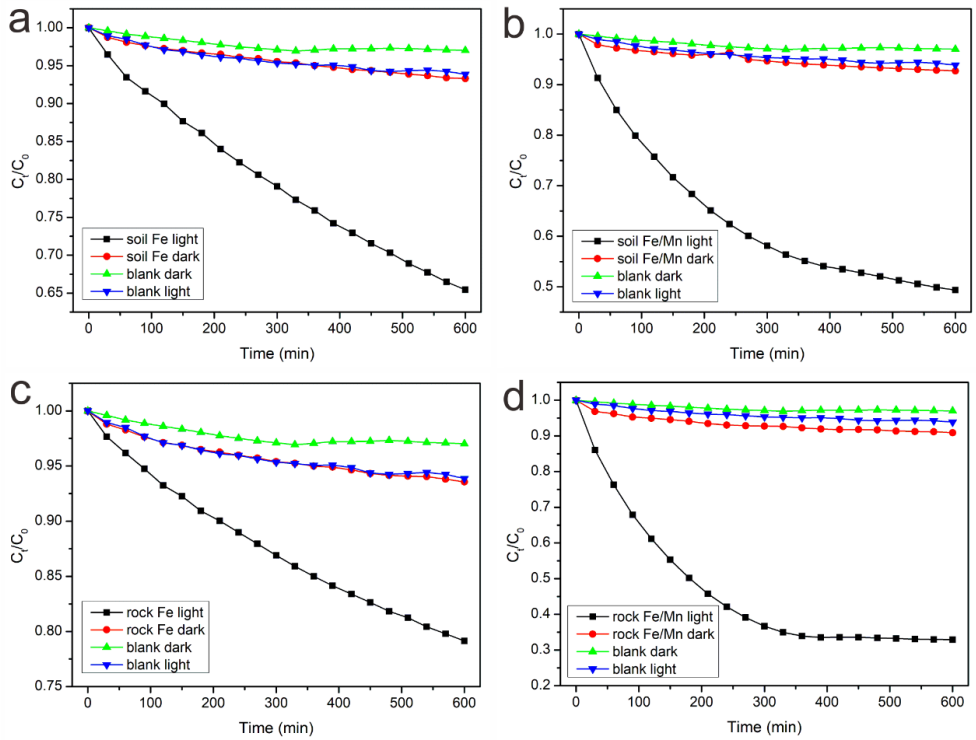

Figure 12. Curves of MO (methyl orange) degradation by the soil Fe coating (**a**), soil Fe/Mn coating (**b**), rock Fe coating (**c**) and rock Fe/Mn coating (**d**) under light irradiation.

Table 1. MO degradation performance of different natural ferromanganese coatings.

Sample	Total Degradation Ratio (%)	Physical Adsorption Ratio (%)	Photocatalysis Degradation Ratio (%)
Soil Fe coating	34.7	6.8	27.9
Soil Fe/Mn coating	50.6	7.3	43.3
Rock Fe coating	20.8	6.5	14.3
Rock Fe/Mn coating	67.2	8.8	58.4

4. Discussion

Chemical reactions catalyzed by minerals have been frequently reported. For example, clay minerals can adsorb organic matters to form RNA, which is important to the origin of life [39] and colloidal (Fe,Ni)S can adsorb α-amino acids and carbon monoxide on its surface to form peptides [40]. Photocatalysis, as one of the most fundamental chemical reactions that happens on mineral surfaces, should have some influence on modern environments as well. In the field of photocatalysis, rutile TiO_2 is the most extensively studied due to its excellent performance. However, the wide band gap of rutile (~3.2 eV) leads to a lack of absorption in the visible portion of the solar light spectrum, which limits its application. In order to increase its photocatalytic activity under visible irradiation, efforts were taken to narrow the band gap of TiO_2 by doping metals and introducing vacancies [41,42]. Furthermore, new photocatalysts with lower band gap energies were alternatively explored [43,44]. For a long time, natural semiconducting Fe/Mn oxide minerals, which are much more abundant than TiO_2, ZnS and WO_3 in storage, have been neglected.

Fe/Mn oxides are common semiconducting minerals that occur in various weathering environments. They can accumulate to form different Fe/Mn-rich coatings under certain conditions. Rock coatings are common in dry arid regions where the pH condition is alkalescent. Soil coatings are common in wet subtropical areas where the pH condition is faintly acid. In this paper, we studied four types of ferromanganese coatings and they displayed different elemental distribution patterns and mineral assemblage. However, in either case, hematite, goethite and birnessite are the major mineral

components in terrestrial ferromanganese coatings. The band gaps of hematite, goethite and birnessite are estimated to be 2.2, 2.6 and 1.82 eV, respectively [45,46]. These minerals are visible-light responsive, i.e., the excitation of photoelectrons from their VBs to CBs can occur under the irradiation wavelength ≤478–683 nm. In geological settings, Fe/Mn oxide minerals continuously absorb solar energy and drive photoredox reactions relevant to the evolution of substances. For example, Fe/Mn oxide minerals can catalyze the formation of ROSs, which can later promote the abiotic oxidation of Mn(II) [47,48] and the decomposition of organic matter [28]. In the euphotic zones of marine and freshwater systems, the photocatalytic self-reduction of birnessite, hematite and goethite serves as a key driver for Mn(II) and Fe(II) ion release [49–51].

The semiconducting properties of natural ferromanganese coatings were studied by laboratory experiments. The photocurrent–time behavior indicates that natural coating electrodes have a good response to irradiation. The ferromanganese coatings can also promote the degradation of MO through photocatalysis. Considering the inhomogeneous chemistry of natural ferromanganese coatings, it is not feasible for us to quantitatively determine the photochemical performance of Fe/Mn oxide minerals. However, among these four types of coatings, the rock Fe/Mn coating, which has a close intergrowth structure of Fe and Mn compounds as observed by EDS mapping (Figure 8), exhibited the best photochemical performance (Figures 11 and 12; Table 1). This phenomenon may be caused by the enhancement of electron–hole separation at the hematite–birnessite interface expected from their band edge position (Figure 13). The CB potentials of birnessite and hematite are −4.37 and −4.87 eV, respectively, while the VB potentials of birnessite and hematite are −6.19 and −7.07 eV, respectively [45,46]. Thus, it is thermodynamically feasible for photoelectrons to transfer from the CB of birnessite to that of hematite, and for holes to transfer from the VB of hematite to that of birnessite (Figure 13). This spatial separation of photo-generated electrons and holes is beneficial to prevent charge recombination, and therefore results in a higher photocatalytic activity [52].

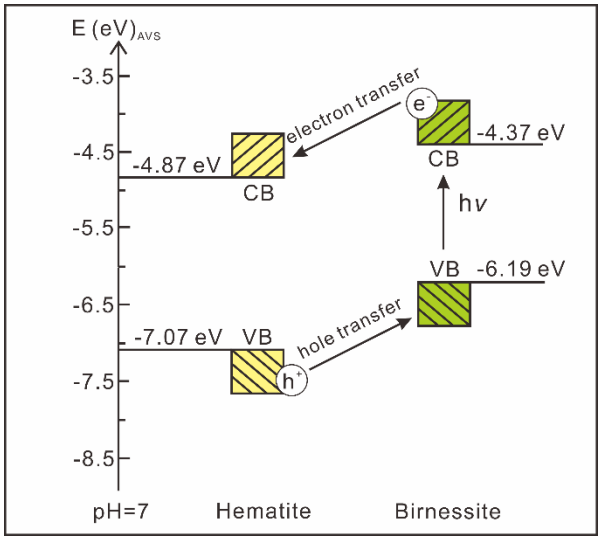

Figure 13. Scheme of the matched band structure of hematite and birnessite in the rock Fe/Mn coating.

Band edges are important parameters to evaluate redox reactions and they can be predicted from the electronegativity of the semiconductor [45]. The CB edge of a compound can be expressed in an absolute vacuum scale (AVS, eV) according to the following equation:

$$E_C = -[X - 1/2E_g + 0.059(pH_{pzc} - pH)] \quad (2)$$

where arameter X is the absolute electronegativity for this compound, E_g stands for the band gap and pH_{pzc} is the pH condition at which a compound demonstrates zero electrical charge on its surface.

Furthermore, the energy position of band edges with respect to the normal hydrogen electrode (NHE) can be converted from the values in the AVS scale using:

$$E(\text{NHE, V}) = -E(\text{AVS, eV}) - 4.5 \quad (3)$$

The specific semiconducting parameters of hematite, goethite and birnessite are listed in Table 2. The curves of the band edge position as a function of pH value are plotted (Figure 14). Irrespective of the faintly acid or alkalescent pH conditions for red soils or arid deserts, the redox potential of humic acid (HA) is well above the VB position of these semiconducting minerals. Humic acid is abundant in almost all environments and it can be oxidized by VB photoholes and separate CB photoelectrons. These free photoelectrons are scavenged by O_2 in the atmosphere, reduce materials in the environment or provide energy sources for bacterial metabolisms [53,54].

Table 2. Absolute electronegativity (X), band gap (E_g) and band edge position (E_v and E_c) of hematite, goethite and birnessite in an AVS (absolute vacuum scale) scale at pH 7.

Minerals	E_g (eV)	E_V (eV)	E_C (eV)	X (eV)	pH_{pzc}	References
hematite	2.2	−7.07	−4.87	5.88	8.6	[45]
goethite	2.6	−7.83	−5.23	6.38	9.7	[45]
birnessite	1.82	−6.19	−4.37	5.59	1.8	[46]

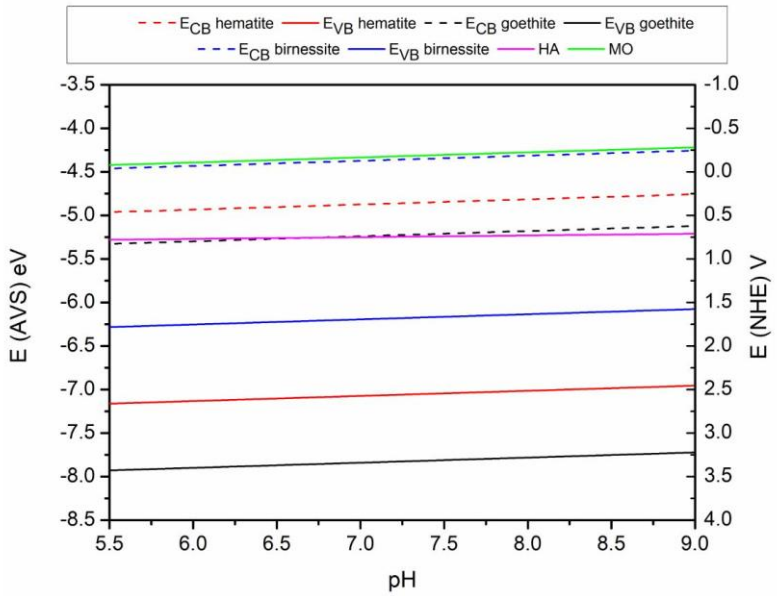

Figure 14. Band edge position of hematite, goethite and birnessite as a function of pH condition. The redox potential of MO and HA (humic acid) [55,56] is above the VB (valence band) position of these minerals, which indicates that MO and HA can serve as photohole scavengers to promote the separation of photoelectrons.

5. Conclusions

Natural terrestrial ferromanganese coatings can develop different mineralogical features. Soil Fe coatings are mainly composed of Al-rich hematite and clays. Soil Fe/Mn coatings can be divided into an outer belt rich in birnessite and an inner belt rich in hematite, goethite, ilmenite and magnetite. Goethite is the only component of rock Fe coatings. Rock Fe/Mn coatings mainly consist of birnessite and hematite, and alternating Fe/Mn-rich and Fe/Mn-poor layers can be discriminated. The photocurrent–time behavior indicates that natural coating electrodes exhibit an immediate increase in photocurrent intensity when exposed to light irradiation. Natural coatings show good performance in the photocatalytic degradation of MO. Under light irradiation, the photocurrent enhancement and organic degradation

efficiency of the rock Fe/Mn coating, which has a close intergrowth structure of Fe and Mn components, is most significant. This phenomenon is attributed to the formation of semiconductor heterojunctions, which can promote the separation of electrons and holes. Terrestrial ferromanganese coatings are common in natural settings and have a good responding capability to visible light irradiation. Therefore, these coatings can exert great influence on surrounding environments by catalyzing important photochemical reactions.

Supplementary Materials: The following are available online at http://www.mdpi.com/2079-6412/10/7/666/s1, Table S1: Chemical compositions of soil Fe coating. Note: b.d.l. = below the detection limit, Table S2: Chemical compositions of the soil Fe/Mn coating. Spots 1–5 are for the outer Mn-rich layer and spots 6–10 are for the inner Fe-rich layer. Note: b.d.l. = below the detection limit, Table S3: Chemical compositions of the rock Fe coating. Note: b.d.l. = below the detection limit, Table S4: Chemical compositions of the rock Fe/Mn coating. Note: b.d.l. = below the detection limit.

Author Contributions: Data curation, X.X. and H.W.; Funding acquisition, A.L.; Methodology, X.X. and H.W.; Resources, Y.L.; Software, H.D.; Supervision, A.L.; Writing—original draft, X.X.; Writing—review and editing, X.X. All authors have read and agreed to the published version of the manuscript.

Funding: This research was funded by the National Natural Science Foundation of China (Grant Nos. 41230103 and 91851208) and the National Key Basic Research Program of China (973 Program, Grant No. 2014CB846001).

Conflicts of Interest: The authors declare no conflict of interest.

References

1. Post, J.E. Manganese oxide minerals: Crystal structures and economic and environmental significance. *Proc. Natl. Acad. Sci. USA* **1999**, *96*, 3447–3454. [CrossRef] [PubMed]
2. Cornell, R.M.; Schwertmann, U. *The Iron Oxides: Structure, Properties, Reactions, Occurrences and Uses*; John Wiley & Sons: Hoboken, NJ, USA, 2003.
3. Ross, S.J.; Franzmeier, D.P.; Roth, C.B. Mineralogy and chemistry of manganese oxides in some indiana soils. *Soil Sci. Soc. Am. J.* **1976**, *40*, 137–143. [CrossRef]
4. Tokashiki, Y.; Dixon, J.B.; Golden, D.C. Manganese oxide analysis in soils by combined X-ray diffraction and selective dissolution methods. *Soil Sci. Soc. Am. J.* **1986**, *50*, 1079–1084. [CrossRef]
5. Tan, W.F.; Liu, F.; Li, Y.H.; He, J.Z.; Li, X.Y. Mineralogy of manganese oxide minerals in iron manganese nodules of several main soils in China. *Pedosphere* **2000**, *10*, 265–274. [CrossRef]
6. Huang, L.; Hong, J.; Tan, W.F.; Hu, H.Q.; Liu, F.; Wang, M.K. Characteristics of micromorphology and element distribution of iron-manganese cutans in typical soils of subtropical China. *Geoderma* **2008**, *146*, 40–47. [CrossRef]
7. Huang, L.; Liu, F.; Tan, W.F.; Hu, H.Q.; Wang, M.K. Geochemical characteristics of selected elements in iron-manganese cutans and matrices of Alfisols in central China. *J. Geochem. Explor.* **2009**, *103*, 30–36. [CrossRef]
8. Potter, R.M.; Rossman, G.R. Desert varnish: The importance of clay minerals. *Science* **1977**, *196*, 1446–1448. [CrossRef]
9. Potter, R.M.; Rossman, G.R. The manganese- and iron-oxide mineralogy of desert varnish. *Chem. Geol.* **1979**, *25*, 79–94. [CrossRef]
10. McKeown, D.A.; Post, J.E. Characterization of manganese oxide mineralogy in rock varnish and dendrites using X-ray absorption spectroscopy. *Am. Mineral.* **2001**, *86*, 701–713. [CrossRef]
11. Garvie, L.A.J.; Burt, D.M.; Buseck, P.R. Nanometer-scale complexity, growth, and diagenesis in desert varnish. *Geology* **2008**, *36*, 215–218. [CrossRef]
12. Xu, X.; Ding, H.; Li, Y.; Lu, A.; Li, Y.; Wang, C. Mineralogical characteristics of Mn coatings from different weathering environments in China: Clues on their formation. *Mineral. Petrol.* **2018**, *112*, 671–683. [CrossRef]
13. Xu, X.; Li, Y.; Li, Y.; Lu, A.; Qiao, R.; Liu, K.; Ding, H.; Wang, C. Characteristics of desert varnish from nanometer to micrometer scale: A photo-oxidation model on its formation. *Chem. Geol.* **2019**, *522*, 55–70. [CrossRef]
14. Lu, A.; Li, Y.; Ding, H.; Xu, X.; Li, Y.; Liang, J.; Liu, Y.; Hong, H.; Chen, N.; Chu, S.; et al. Photoelectric conversion on Earth's surface via widespread Fe- and Mn-mineral coatings. *Proc. Natl. Acad. Sci. USA* **2019**, *116*, 9741–9746. [CrossRef]

15. Perry, R.S.; Adams, J.B. Desert varnish: Evidence for cyclic deposition of manganese. *Nature* **1978**, *276*, 489–491. [CrossRef]
16. Liu, T.; Broecker, W.S. Millennial-scale varnish microlamination dating of late Pleistocene geomorphic features in the drylands of western USA. *Geomorphology* **2013**, *187*, 38–60. [CrossRef]
17. Lee, M.R.; Bland, P.A. Dating climatic change in hot deserts using desert varnish on meteorite finds. *Earth Planet. Sci. Lett.* **2003**, *206*, 187–198. [CrossRef]
18. Tan, W.F.; Liu, F.; Feng, X.H.; Huang, Q.Y.; Li, X.Y. Adsorption and redox reactions of heavy metals on Fe–Mn nodules from Chinese soils. *J. Colloid Interface Sci.* **2005**, *284*, 600–605. [CrossRef]
19. Sherman, D.M. Electronic structures of iron(III) and manganese(IV) (hydr)oxide minerals: Thermodynamics of photochemical reductive dissolution in aquatic environments. *Geochim. Cosmochim. Acta* **2005**, *69*, 3249–3255. [CrossRef]
20. Zaied, M.; Chutet, E.; Peulon, S.; Bellakhal, N.; Desmazières, B.; Dachraoui, M.; Chaussé, A. Spontaneous oxidative degradation of indigo carmine by thin films of birnessite electrodeposited onto SnO_2. *Appl. Catal. B Environ.* **2011**, *107*, 42–51. [CrossRef]
21. Ye, Q.; Lu, H.; Zhao, J.; Cheng, S.; Kang, T.; Wang, D.; Dai, H. A comparative investigation on catalytic oxidation of CO, benzene, and toluene over birnessites derived from different routes. *Appl. Surf. Sci.* **2014**, *317*, 892–901. [CrossRef]
22. Hou, J.; Li, Y.; Mao, M.; Ren, L.; Zhao, X. Tremendous effect of the morphology of birnessite-type manganese oxide nanostructures on catalytic activity. *ACS Appl. Mater. Interfaces* **2014**, *6*, 14981–14987. [CrossRef] [PubMed]
23. Chien, S.W.C.; Chen, H.L.; Wang, M.C.; Seshaiah, K. Oxidative degradation and associated mineralization of catechol, hydroquinone and resorcinol catalyzed by birnessite. *Chemosphere* **2009**, *74*, 1125–1133. [CrossRef]
24. Nakayama, M.; Shamoto, M.; Kamimura, A. Surfactant-induced electrodeposition of layered manganese oxide with large interlayer space for catalytic oxidation of phenol. *Chem. Mater.* **2010**, *22*, 3584–3593. [CrossRef]
25. Zhang, H.; Ding, H.; Wang, X.; Zeng, C.; Lu, A.; Li, Y.; Wang, C. Photoelectrochemical performance of birnessite films and photoelectrocatalytic activity toward oxidation of phenol. *J. Environ. Sci.* **2017**, *52*, 259–267. [CrossRef] [PubMed]
26. Wiechen, M.; Zaharieva, I.; Dau, H.; Kurz, P. Layered manganese oxides for water-oxidation: Alkaline earth cations influence catalytic activity in a photosystem II-like fashion. *Chem. Sci.* **2012**, *3*, 2330–2339. [CrossRef]
27. Robinson, D.M.; Go, Y.B.; Mui, M.; Gardner, G.; Zhang, Z.J.; Mastrogiovanni, D.; Garfunkel, E.; Li, J.; Greenblatt, M.; Dismukes, G.C. Photochemical water oxidation by crystalline polymorphs of manganese oxides: Structural requirements for catalysis. *J. Am. Chem. Soc.* **2013**, *135*, 3494–3501. [CrossRef]
28. Georgiou, C.D.; Sun, H.J.; Mckay, C.P.; Grintzalis, K.; Papapostolou, I.; Zisimopoulos, D.; Panagiotidis, K.; Zhang, G.; Koutsopoulou, E.; Christidis, G.E.; et al. Evidence for photochemical production of reactive oxygen species in desert soils. *Nat. Commun.* **2015**, *6*, 7100. [CrossRef]
29. Shinde, S.K.; Dubal, D.P.; Ghodake, G.S.; Fulari, V.J. Electronic impurities (Fe, Mn) doping in CdSe nanostructures for improvements in photoelectrochemical applications. *RSC Adv.* **2014**, *4*, 33184–33189. [CrossRef]
30. Shinde, S.K.; Dubal, D.P.; Ghodake, G.S.; Lee, L.S.; Lohar, G.M.; Rath, M.C.; Fulari, V.J. Baking impact of Fe composition on CdSe films for solar cell application. *Mater. Lett.* **2014**, *132*, 243–246. [CrossRef]
31. Kwon, K.D.; Refson, K.; Sposito, G. On the role of Mn(IV) vacancies in the photoreductive dissolution of hexagonal birnessite. *Geochim. Cosmochim. Acta* **2009**, *73*, 4142–4150. [CrossRef]
32. Potter, R.M.; Rossman, G.R. The tetravalent manganese oxides: Identification, hydration, and structural relationships by infrared spectroscopy. *Am. Mineral.* **1979**, *64*, 1199–1218.
33. Julien, C.M.; Massot, M.; Poinsignon, C. Lattice vibrations of manganese oxides—Part 1. Periodic structures. *Spectrochim. Acta Part A* **2004**, *60*, 689–700. [CrossRef]
34. Li, Y.; Lu, A.H.; Wang, C.Q.; Wu, X.L. Characterization of natural sphalerite as a novel visible light-driven photocatalyst. *Sol. Energy Mater. Sol. Cells* **2008**, *92*, 953–959. [CrossRef]
35. De Faria, D.L.A.; Silva, S.V.; Oliveira, M.T.D. Raman microspectroscopy of some iron oxides and oxyhydroxides. *J. Raman Spectrosc.* **1997**, *28*, 873–878. [CrossRef]
36. Beattie, I.R.; Gilson, T.R. The single-crystal Raman spectra of nearly opaque materials. Iron (III) oxide and chromium (III) oxide. *J. Chem. Soc.* **1970**, *1*, 980–986. [CrossRef]

37. Zoppi, A.; Lofrumento, C.; Castellucci, E.M.; Sciau, P. Al-for-Fe substitution in hematite: The effect of low Al concentrations in the Raman spectrum of Fe_2O_3. *J. Raman Spectrosc.* **2008**, *39*, 40–46. [CrossRef]
38. Dias, A.; Sá, R.G.; Spitale, M.C.; Athayde, M.; Ciminelli, V.S.T. Microwave-hydrothermal synthesis of nanostructured Na-birnessites and phase transformation by arsenic(III) oxidation. *Mater. Res. Bull.* **2008**, *43*, 1528–1538. [CrossRef]
39. Ferris, J.P. Mineral catalysis and prebiotic synthesis: Montmorillonite-catalyzed formation of RNA. *Elements* **2005**, *1*, 145–149. [CrossRef]
40. Huber, C.; Eisenreich, W.; Hecht, S.; Wächtershäuser, G. A possible primordial peptide cycle. *Science* **2003**, *301*, 938–940. [CrossRef]
41. Umebayashi, T.; Yamaki, T.; Itoh, H.; Asai, K. Analysis of electronic structures of 3d transition metal-doped TiO_2 based on band calculations. *J. Phys. Chem. Solids* **2002**, *63*, 1909–1920. [CrossRef]
42. Morgan, B.J.; Watson, G.W. A density functional theory + U study of oxygen vacancy formation at the (110), (100), (101), and (001) surfaces of rutile TiO_2. *J. Phys. Chem. C* **2009**, *113*, 7322–7328. [CrossRef]
43. Spichiger-Ulmann, M.; Augustynski, J. Aging effects in n-type semiconducting WO_3 films. *J. Appl. Phys.* **1983**, *54*, 6061–6064. [CrossRef]
44. Shinde, S.S.; Sami, A.; Lee, J.H. Sulfur mediated graphitic carbon nitride/S-Se-graphene as a metal-free hybrid photocatalyst for pollutant degradation and water splitting. *Carbon* **2016**, *96*, 929–936. [CrossRef]
45. Xu, Y.; Schoonen, M.A.A. The absolute energy positions of conduction and valence bands of selected semiconducting minerals. *Am. Mineral.* **2000**, *85*, 543–556. [CrossRef]
46. Liu, F.F.; Li, Y.; Ding, H.R.; Ding, C.; Lu, A.H. Researches on the band structure of several types of manganese oxides. *Bull. Miner. Petrol. Geochem.* **2017**, *36*, 476–482. (In Chinese with English abstract) [CrossRef]
47. Learman, D.R.; Wankel, S.D.; Webb, S.M.; Martinez, N.; Madden, A.S.; Hansel, C.M. Coupled biotic–abiotic Mn(II) oxidation pathway mediates the formation and structural evolution of biogenic Mn oxides. *Geochim. Cosmochim. Acta* **2011**, *75*, 6048–6063. [CrossRef]
48. Lan, S.; Wang, X.; Xiang, Q.; Yin, H.; Tan, W.; Qiu, G.; Liu, F.; Zhang, J.; Feng, X. Mechanisms of Mn(II) catalytic oxidation on ferrihydrite surfaces and the formation of manganese (oxyhydr)oxides. *Geochim. Cosmochim. Acta* **2017**, *211*, 79–96. [CrossRef]
49. Sunda, W.G.; Huntsman, S.A.; Harvey, G.R. Photoreduction of manganese oxides in seawater and its geochemical and biological implications. *Nature* **1983**, *301*, 234–236. [CrossRef]
50. Wells, M.L.; Mayer, L.M.; Donard, O.F.X.; Sierra, M.M.D.S.; Ackelson, S.G. The photolysis of colloidal iron in the oceans. *Nature* **1991**, *353*, 248–250. [CrossRef]
51. Delgadillo-Hinojosa, F.; Segovia-Zavala, J.A.; Huerta-Díaz, M.A.; Atilano-Silva, H. Influence of geochemical and physical processes on the vertical distribution of manganese in Gulf of California waters. *Deep Sea Res.* **2006**, *53*, 1301–1319. [CrossRef]
52. Wang, Y.; Wang, Q.; Zhan, X.; Wang, F.; Safdar, M.; He, J. Visible light driven type II heterostructures and their enhanced photocatalysis properties: A review. *Nanoscale* **2015**, *5*, 8326–8339. [CrossRef] [PubMed]
53. Lu, A.; Li, Y.; Jin, S.; Wang, X.; Wu, X.; Zeng, C.; Li, Y.; Ding, H.; Hao, R.; Lv, M.; et al. Growth of non-phototrophic microorganisms using solar energy through mineral photocatalysis. *Nat. Commun.* **2012**, *3*, 768. [CrossRef] [PubMed]
54. Sakimoto, K.K.; Wong, A.B.; Yang, P. Self-photosensitization of nonphotosynthetic bacteria for solar-to-chemical production. *Science* **2016**, *351*, 74–77. [CrossRef] [PubMed]
55. Struyk, Z.; Sposito, G. Redox properties of standard humic acids. *Geoderma* **2001**, *102*, 329–346. [CrossRef]
56. Zang, L.; Liu, C.Y.; Ren, X.M. Photochemistry of semiconductor particles 3. Effects of surface charge on reduction rate of methyl orange photosensitized by ZnS sols. *J. Photochem. Photobiol. A* **1995**, *85*, 239–245. [CrossRef]